FIRST DETECTION OF MAGNETIC FIELDS IN A DARK CLOUD FROM SPACE: ISO FAR-INFRARED POLARIMETRY OBSERVATIONS OF GF9

D. Clemens[1], K. Kraemer[1], and D. Ciardi[2]

[1]Institute for Astrophysical Research, Boston University, USA.
[2]Department of Astronomy, University of Florida, USA.

ABSTRACT

ISO was used to perform far-infrared polarimetry of the thermal dust emission from the filamentary dark cloud GF9 using the PHT instrument and C_160 filter. Embedded magnetic fields within the GF9 cloud were sought using linear polarization probes of a dense core region, a diffuse filamentary region, and two reference regions. The observations utilized the ISOPHT C200 2×2 pixel camera and took the form of small, overlapping raster maps with each central sky position being viewed by each of the camera pixels.

The magnetic fields contained within this dark cloud were directly detected – the first such detections using space-based techniques. Polarized dust emission was detected from the dense core, the filament, and one reference region. The average degree of polarization found was about 5%. The polarization properties of the two regions within the GF9 cloud are completely different, however. The star-forming dense core (containing the Class 0 source IRAS PSC 20503+6006) shows exceedingly parallel polarization vectors, revealing a highly uniform embedded magnetic field. The non-star forming filament shows very disordered magnetic field directions, possibly indicating that magnetic turbulence may be important in supporting some dense cores against collapse.

Key words: ISO; infrared astronomy; polarimetry; magnetic fields.

1. INTRODUCTION

Magnetic fields are thought to be important to the star formation process, but are exceedingly difficult to measure. Background starlight polarization techniques at optical wavelengths (e.g. Goodman et al. 1990) may be unable to probe magnetic fields in cold, dark regions in molecular clouds and cloud cores. A more direct probe of embedded magnetic fields is to use far-infrared linear polarimetry of the spinning, aligned dust grains within the clouds (e.g. Novak et al. 1997).

It is also important to be able to probe for magnetic fields in regions of low-mass star formation, where the magnetic field signatures and structures might survive the star formation process. However, the Kuiper Airborne Observatory (KAO) and its replacement, SOFIA, are sensitivity-limited to polarimetric probes of only the brightest regions of the brighest star forming sites. Only a space-based far-infrared polarimetric capable observatory such as *ISO* can sense magnetic fields in the fainter, more quiescent low-mass forming cloud cores.

Finally, a direct comparison of the magnetic field properties of star-forming and starless regions in the same dark cloud would reveal the role played by the field in forming low-mass stars.

In the following, our ISOPHT polarimetric observations of the filamentary dark cloud GF9 are described. The observations used the C_160 filter and were made as small "mini-maps" with each C200 camera pixel viewing the target directions. Analysis of the data consisted of standard PIA processing, with a few non-standard options selected, followed by polarimetric analysis of the *ISO* signals using custom software. Using our observations and analysis, we independently measured the instrumental polarizations of the C200 pixels, finding good agreement with the published values contained in Klaas et al. (1999). In the following, we describe the observations, the data reduction, the analyses performed, and summarize the polarimetric and photometric results obtained for GF9.

2. ISOPHT OBSERVATIONS

The GF9 cloud is seen in the digital version of the Palomar Sky Survey as the band of mostly star-free material stretching from the lower right to upper left corners of Figure 1. The locations of the centers of the "Core" (L1082C) and "Filament" regions studied here are indicated on the Figure, as are two reference observing positions ("C-Off" and "F-Off") chosen to sample roughly the same lines of sight, but not intercepting the optically opaque or *IRAS*-traced GF9 cloud material.

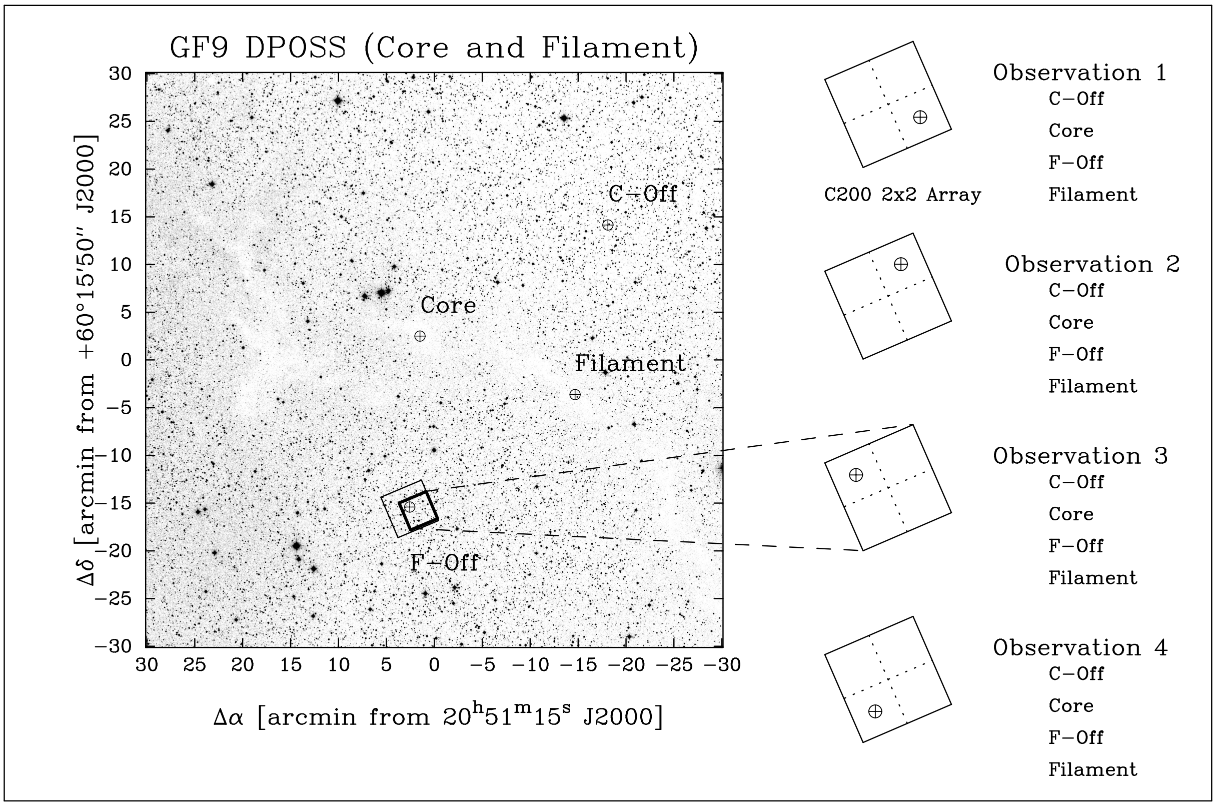

Figure 1. Digital Palomar Sky Survey image containing the GF9 filamentary dark molecular cloud. On the image, the circled crosses show the four sky regions toward which small polarimetric maps were obtained by ISO, identified as "Core," "Filament," "C-Off," and "F-Off." The observational scheme is outlined on the right side of the figure, showing that each sky region was sampled by each of the four C200 pixels. The box located in the lower right of the image shows the size of the area covered by the small polarimetric maps and the instantaneous size of one field of view of the C200 2×2 *pixel camera.*

2.1. ISO Photometric Observations

The Core and Filament regions were mapped using ISOPHT to develop far-infrared maps capable of revealing the dust temperatures of these two regions. Each region was mapped using the C_70, C_100, C_135, and C_200 filters in the PHT32 AOT. The Core C_70 and Filament C_200 filter maps show that the structure seen in Fig. 1 is also seen in the far-infrared and should provide a reasonable guide for interpreting the polarization results.

2.2. ISO Polarimetric Observations

Four regions toward GF9 were observed using the PHT 2×2 pixel C200 array detector and the C_160 filter (mean wavelength $184\,\mu$m, width $50\,\mu$m) on the 22 February 1998 orbit. The observing strategy is summarized in the right column of Fig. 1. It involved pointing *ISO* such that Pixel 1 in the C200 array was centered consecutively on the Core central location (defined for the polarimetric observations to be the *IRAS* PSC 20503+6006 position), the C-Off location, the Filament location, and finally the F-Off location. This cycle of *ISO* pointings was then repeated for each of the other three C200 pixels. Using this scheme, a 3×3 "mini-map" of sky positions was observed toward each of the four sky regions, with the central position of each region having been observed with *each* of the C200 pixels (see inset on Fig. 1). In addition, four of the nine sky positions toward each region were observed with two of the C200 pixels.

At each pointing of *ISO*, the PHT51 AOT for collecting polarimetry data involved a 128 second measurement through the 0° angle polarization filter (a fixed-angle wire grid), followed by 128 second measurements through the 120° and 240° polarization filters. This three-filter cycle was performed a second time, followed by a 128 second measurement through the "open" filter position (no wire grid). After these seven data collection periods, the Fine Calibration Source (FCS) was turned on and measured by the C200 camera before *ISO* moved to point to the next sky region. For each 128 s measurement, the 1/8 s destructive readout (DR) cycle time of each of the four C200 pixels yielded 1024 "data ramps" of integrated detector voltage versus time. Each data ramp was sampled non-destructively at three different times and destructively once.

3. DATA PROCESSING

Data processing involved developing surface brightness values for each staring observation through the wire grid polarimetric filters while preserving the high S/N necessary for performing polarimetric analyses.

Under standard PIA data processing, the first and last samples (readouts) of each integration ramp are discarded, and the source flux is determined from the slope of the remaining points as obtained from a linear fit. This yielded S/N values around 160 for our data. Instead, we selected the PIA option in the ERD processing to include *all* good data points in the slope fitting of each ramp. This lead to S/N values of 900, which agreed with measured sample variances.

Other ERD-level corrections included the ramp linearity correction, glitch editing using the "two-threshold" technique with more aggressive 3σ limits compared to the standard 4.5σ limits, and linear fitting of the remaining integration ramps. SRD-level corrections included accounting for the destructive readout reset interval, the dark current correction, and further glitch editing – again with an aggressive threshold which removed both low and high aberrant ramp slopes.

In processing the data from the SRD to SCP level, drift handling was employed to average only those ramp slopes measured after detector stabilization had occurred. Depending on the pixel and its illumination history, the percentage of retained ramp slope values averaged about 50%, but varied from about 10% to 90% and was a source of pixel-to-pixel variation in the final S/N values. In forming the final signals (the average retained integration ramp slope values), both weighted and unweighted averages were calculated. These were found to be quite similar, with only a modest bias in the weighted averages. To be conservative, the unweighted average signals were used in the polarimetric analysis.

The FCS observations were similarly corrected. The corrected FCS observations were used to establish the "actual responsivities" and these were applied to each wire grid filter observation on a pointing-by-pointing basis to yield fully calibrated surface brightness values. Figure 2 shows the resulting signals versus a consecutive (time ordered) observation number index.

In Fig. 2, the bottom panel contains labels which identify each set of six data points as corresponding to the two cycles through the three wire grid filters and the repeated pointing sequence through the four observing regions: C-Off, Core, F-Off, and Fila. The "open" (no wire grid) filter values have been omitted to highlight the wire grid values. Note that the Core surface brightness is greatest in Pixel 1 (top panel) during the first set of four pointings, is greatest in Pixel 2 during the second set of four pointings, and so on for Pixels 3 and 4. These correspond to *ISO* being pointed so that the bright Core source PSC 20503+6006 was centered within each of the indicated pixels. Patterns are seen in the signals measured through the 0°, 120°, and 240° wire grids which repeat from one set of three measurements to the next. This "triplet" pattern persists for all pointings of each pixel and are due to instrumental polarization.

The reduced polarimetric filter-photometric data show S/N values of about 800-1100:1. This is quite sufficient for the detection of the weak linear polarizations ($\sim$ 1 to 10%) expected from magnetically-aligned thermally-emitting dust grains.

3.1. Polarimetric Analysis

Analysis of the ISOPHT polarimetric data consisted of four steps: (1) evaluation of the instrumental polarizations, (2) computation of the differences in surface brightness seen toward each target zone compared to a reference zone for each polarimetric filter configuration, (3) computation of the normalized Stokes u and q values seen by each camera pixel for each such difference observation, and (4) computation of a least squares solution of the u and q values for each "sky pixel" from the overlapping, multi-pixel observations.

3.1.1. Instrumental Polarizations

Klaas et al. (1999, hereafter KLC) report measured instrumental polarizations for the four C200 pixels. Their values of instrumental percentage polarizations are between 3.4 and 6.1%, with uncertainties of the order of 0.3%.

Our faint "C-Off" position was chosen as a reference of background surface brightness and used to compute trial instrumental polarizations. The underlying assumption is that the C-Off region exhibits a spatially smooth background flux with no net linear polarization. The observed C-Off surface brightness values were converted to Stokes parameters from the values measured through the three wire grid filters (0°, 120°, 240°) in the usual way. The Stokes U and Q values were divided by the I value and the measured polarizer efficiency (90 ± 3%, KLC) to form the normalized Stokes parameters u and q, which were used to calculate instrumental percentage polarizations and position angles, in the instrument system. Table 1 presents these C-Off instrumental polarizations. Comparison of these C-Off values to the KLC values shows a generally high degree of agreement. We conclude that the instrumental polarizations for ISOPHT are stable enough to warrant use of the KLC values to correct our observed polarizations.

Table 1. ISOPHT Instrumental Polarizations computed from C-Off Values.

Pixel	$P_{\rm Instrument}$ [%]	$\theta_{\rm Instrument}$ [°]
1	6.7 ± 0.3	-65.3 ± 1.5
2	7.0 ± 0.5	-89.9 ± 2.0
3	7.0 ± 0.4	-46.3 ± 1.5
4	1.4 ± 0.5	-74.5 ± 10.7

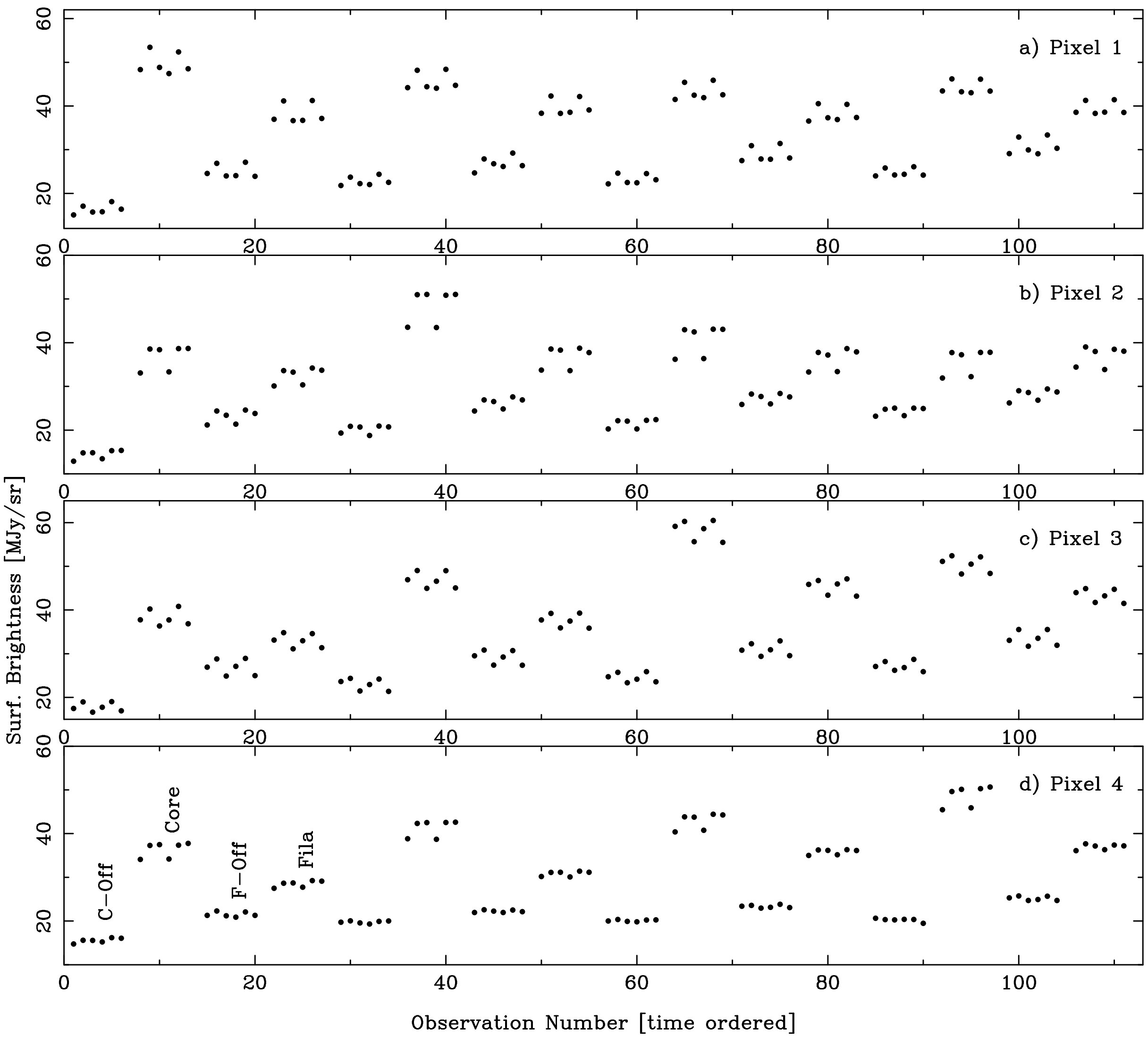

Figure 2. Summary of the reduced data set for this study, displayed as values of measured surface brightness versus observation number, a consecutive time index of the polarimetric observations. The four panels a - d display data for each of the four C200 camera pixels. The "open" filter observations have been omitted.

3.1.2. Sky Polarizations

Analysis of the polarization data toward the Core, Fila, and F-Off regions began with the formation of first differences of the surface brightness of each region relative to those of the C-Off region. The surface brightness first differences were formed by subtracting the C-Off signals from the target (Core, Fila, or F-Off) signals – all within the same cycle of pointings, for the same pixels, for the same polarizer filters in order to remove the remaining first order responsivity drifts seen in Fig. 2. The resulting excess surface brightness values seen through the polarizer filters were combined to form Stokes I, U, and Q and their uncertainties, and normalized as before to form u and q. Instrumental polarization corrections were applied, utilizing the KLC values. The instrumental polarization-corrected Stokes u and q for the four separate observations of each region (viewing of the central sky position by each of the four C200 pixels) were combined in a least squares approach to solve for the sky Stokes parameters for the 9 sky pixels for each of the Core, Fila, and F-Off target zones.

Surface brightness maps through the C_160 filter for the three regions observed polarimetrically were derived during this analysis and are shown as color scale pixel maps (with reference surface brightness calibration scales) in Figures 3a, 3b, and 3c. The sky pixel numbering scheme is shown in Figure 3d. The calculated sky pixel polarizations are shown on Figure 3 as vectors whose lengths are proportional to the percentage polarizations and whose position angles correspond to the inferred *magnetic field* directions. The polarization uncertainties are limited more by uncertainties in the instrumental polarization (of value 0.3% – KLC) than by the internal uncertainties of the observations themselves.

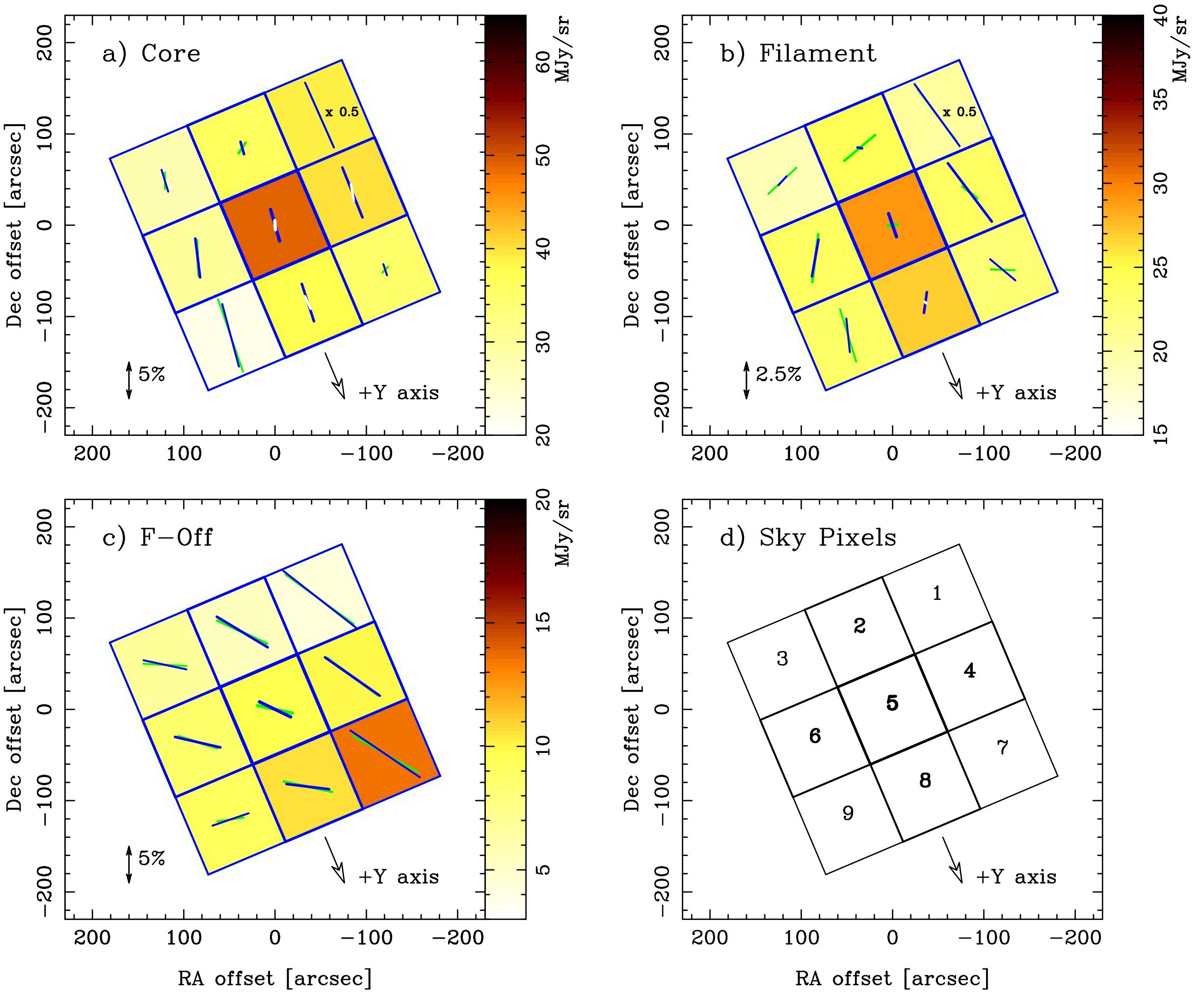

Figure 3. *Surface brightness and polarization maps obtained by ISOPHT in the C_160 filter toward the three sky regions. (a) (Upper left) Core region map; (b) (Upper right) Filament region map; (c) (Lower left) F-Off region map; (d) (Lower right) Convention for the identification of sky pixels. Each region map shows the total surface brightness as different color levels and the measured polarizations as vectors. Vector lengths are proportional to the percentage polarizations measured. Vector directions show the inferred magnetic field direction on the sky, and are 90° rotated from the measured polarization position angle directions. Blue vectors show values obtained using the KLC instrumental polarizations; green and white vectors show values obtained from the C-Off instrumental polarizations. In the Core and Filament maps, the polarization percentages for Sky Pixel 1 have been reduced in length a factor of 2.*

4. DISCUSSION

Polarization from thermally emitting dust grains in the GF9 cloud was detected by *ISO* with a high degree of confidence, as shown Figure 3. Of the 27 sky positions surveyed, 21 showed linear polarizations detected with more than 5:1 S/N. The lowest polarization uncertainties, about 0.2%, were obtained toward the centers of the Core and Filament maps. Hence, *direct detection of the magnetic fields contained within a dark cloud using space-based techniques has been performed for the first time.*

Within the GF9 cloud, the physical natures of the Core and Filament regions were compared to test for relationships between magnetic field properties and star formation conditions. In comparing the *ISO* polarization results for the Core and Filament, three new and compelling facts arise: 1) the star-forming Core region contains an exceedingly ordered (highly parallel) magnetic field, 2) the direction of the magnetic field in the Core is nearly parallel to the line connecting the YSO PSC 20503+6006 with the nearby dense, but as yet starless, cloud core seen at 100 μm in *IRAS* HIRES images and ISOPHT far-infrared maps, the magnetic field in the starless Filament is highly disordered.

The Core region toward PSC 20503+6006 shows a highly ordered magnetic field with a measured directional dispersion under 5°. The starless Filament region shows a highly disordered magnetic field, both in direction and in degree of polarization. The polarization directions in the Filament show a directional dispersion of 21°. Interestingly, the F-Off region also shows a highly ordered magnetic field. The degree of polarization is high across the entire F-Off region and the directional dispersion is quite low (∼11°). This is not an instrumental polarization artifact, as examination of Fig. 2 shows the F-Off data triplet shapes to be distinctly different from the triplets for the C-Off, Core, and Fila regions.

The F-Off region shows a higher mean polarization percentage than the Filament region, although both regions show similar linearly polarized surface brightness (0.3-0.5 MJy sr^{-1}). The Core values are about five times larger, much in excess of the higher relative surface brightness values of the Core. This argues against these polarizing dust grains being distributed as a thin layer or skin around the Core region and instead requires that the emitting and polarizing dust be well-mixed.

With the discovery that the magnetic field contained in the Core region is highly ordered and likely related to the star formation process taking place there, a number of existing observations were combined to develop a broad spectral energy distribution (SED) for the PSC source and its nature reevaluated. ISOPHT PHT32 data for the C_70, C_100, C_135, and C_200 filters were combined with the PHT51 C_160 filter data and existing *IRAS* flux values and are shown in Figure 4.

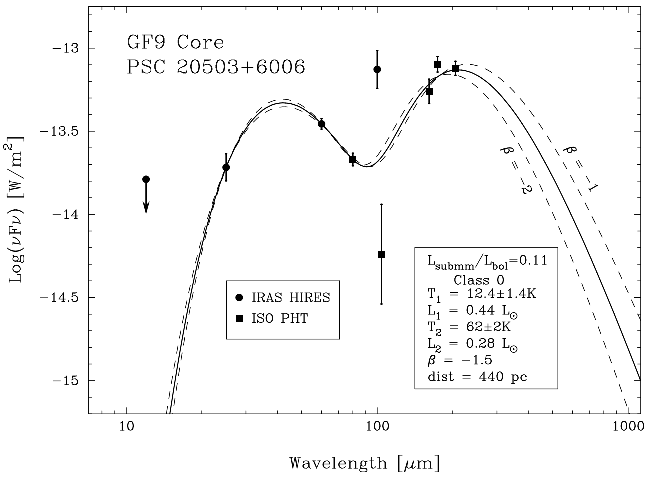

Figure 4. Measured and modeled spectral energy distributions for PSC 20503+6006. Data points indicated as filled circles are from analysis of IRAS HIRES images, with the 12 μm point representing the FSC upper limit. Filled squares represent fluxes obtained from GF9 ISOPHT photometric and polarimetric maps and are plotted along the horizontal axis at the effective wavelengths of the observations. Error bars are ±1 σ in length. The solid line represents a two blackbody fit to these data, with a dust emissivity power law index β set equal to −1.5. Dashed lines represent β = −1 and −2 fits, as indicated. The legend summarizes the β = −1.5 fit values.

A two component model of the SED was used to fit the temperatures and luminosities for two blackbodies, both of which have optically thin dust emissivities exhibiting power law scalings with wavelength. The model for the power law index $\beta = -1.5$ is shown as the solid line in Fig. 4. This fit was integrated for $\lambda > 350\,\mu$m to find $L_{submm} = 0.083\,L_\odot$ and the ratio $L_{submm}/L_{bol} = 0.11$, where $L_{bol} = 0.73\,L_\odot$ contains both cold and warm SED components. Ratios this high characterize extreme Class 0 sources such as VLA 1623 (André et al. 1993).

5. SUMMARY

ISOPHT was used to conduct a C_160 far-infrared polarimetric investigation of two regions in the filamentary dark cloud GF9. Significant linear polarizations due to magnetic alignment of thermally emitting dust grains in the cloud were detected. The magnetic field was found to be highly ordered in the star forming site and highly disordered in the quiescent site. The magnetic field direction in the star forming site appears to connect this region to a nearby dense core which has not yet formed stars. Combining *IRAS* and *ISO* fluxes from 12 to 200μm, the SED was developed for the young stellar object in the star forming site PSC 20503+6006. This $0.73 L_\odot$ SED is well-fit by a model containing two blackbodies modified by an emissivity with the usual power law index. The SED and model fit indicate $L_{submm}/L_{bol} \sim 0.11$; hence, a Class 0 designation for this object is appropriate.

The association of a region of highly ordered magnetic field with the youngest stage of star formation, and the association of a disordered field with a lack of star formation for an otherwise identical dense cloud core, represent compelling evidence for a critically important role of the magnetic field in the star formation process.

ACKNOWLEDGEMENTS

This study was based on observations made with *ISO*, an European Space Agency (ESA) project with instruments funded by ESA Member States (especially the PI countries: France, Germany, the Netherlands, and the United Kingdom) and with the participation of ISAS and NASA. The ISOPHT data presented here were reduced using PIA, which is a joint development by the ESA Astrophysics Division and the ISOPHOT consortium. The Digitized Sky Survey was produced at the Space Telescope Science Institute (STScI) under U.S. Government grant NAG W-2166. The image shown here was based on photographic data obtained using Oschin Schmidt Telescope on Palomar Mountain. The Palomar Observatory Sky Survey was funded by the National Geographic Society. The Oschin Schmidt Telescope is operated by the California Institute of Technology and Palomar Observatory. The plates were processed into the present compressed digital format with their permission. Ulrich Klaas (MPIfA) spent countless hours characterizing and describing the PHT instrumental polarization program and observations. Paul Bowen performed the PIA reductions of the *ISO* photometric data at Boston University. Analysis of *ISO* data at Boston University was supported by NASA grants NAG5-3337, JPL-961513, and JPL-1207131.

REFERENCES

André, P., Ward-Thompson, D., & Barsony, M. 1993, ApJ, 406, 122

Goodman, A. A., Bastien, P., Menard, F., & Myers, P. C. 1990, ApJ, 359, 363

Klaas, U., Laureijs, R. J., & Clavel, J. 1999, ApJ, 512, 157

Novak, G., Dotson, J. L., Dowell, C. D., Goldsmith, P. F., Hildebrand, R. H., Platt, S. R., & Schleuning, D. A. 1997, ApJ, 487, 320